THE ASTROPHYSICAL JOURNAL SUPPLEMENT SERIES, 108:279–299, 1997 January

THE DOMINION RADIO ASTROPHYSICAL OBSERVATORY GALACTIC PLANE SURVEY PILOT PROJECT: THE W3/W4/W5/HB 3 REGION

M. NORMANDEAU AND A. R. TAYLOR
Department of Physics and Astronomy, University of Calgary, 2500 University Drive NW, Calgary, AB T2N 1N4, Canada
AND
P. E. DEWDNEY
Dominion Radio Astrophysical Observatory, National Research Council of Canada, Box 248, Penticton, BC V2A 6K3, Canada
Received 1996 May 8; accepted 1996 August 6

ABSTRACT

The Dominion Radio Astrophysical Observatory, in collaboration with other sites, recently began a Galactic plane survey. The data from the pilot project for this survey are presented here. They cover the W3/W4/W5/HB 3 Galactic complex in the Perseus arm. Ten fields were observed to produce mosaic images of this region at two continuum frequencies, 408 and 1420 MHz, as well as in the 21 cm spectral line of atomic hydrogen at 127 velocities covering +55.5 to −153.9 km s^{-1}. At 1420 MHz (continuum and spectral line), an area of approximately 8° × 6° ($l \times b$) is imaged with a resolution of 1.′00 × 1.′14 (east-west by north-south) whereas, at 408 MHz, the coverage was 14° × 10° ($l \times b$) with a resolution of 3.′5 × 4.′0 (east-west by north-south). The spectral-line data cube constitutes the highest resolution atomic hydrogen study of the entire complex to date. A wealth of large-scale filaments, arcs, bubbles, and shells is revealed.

Subject headings: H II regions — ISM: clouds — radio continuum: ISM — radio lines: ISM — surveys

1. INTRODUCTION

The Dominion Radio Astrophysical Observatory (DRAO) recently began observations for a survey of the northern Galactic plane with its synthesis telescope. This survey will provide images of the Galactic plane in the longitude interval 75°–145° and latitude range −3° to +5° by constructing a mosaic from a large number (186) of individual synthesis fields. The observations will yield an atomic hydrogen (H I) spectral-line data cube with 256 velocity channels and angular resolution of ∼1′. At the same time, continuum images at 1420 and 408 MHz will be obtained, with full polarization data at 1420 MHz. Observations began in 1995 March and will continue for approximately 4 years.

Prior to undertaking such a project, its feasibility needed to be ascertained. To this end, a pilot survey was conducted in 1993. Observations of the W3/W4/W5/HB 3 Galactic complex were carried out in June, July, November, and December of that year.

The W3/W4/W5/HB 3 Galactic complex in the Perseus spiral arm, associated with the Cas OB6 association, includes the open star clusters OCl 352 and OCl 364, the H II regions W3 (IC 1795), W4 (IC 1805, S190), and W5 (IC 1848, S199), a giant molecular cloud, a complex of dust clouds, and the supernova remnant (SNR) HB 3. To orient the reader, the main constituents of the complex are outlined in Figure 1; the positions of 3C 58, 3C 69, and Maffei 2 are also indicated, as these will be mentioned later. W3, W4, and W5 form a chain of H II regions that frequently serve as a test bed for the study of OB star formation in our Galaxy. Their spatial orientation is such that there is very little overlap along the line of sight among the various components providing information about star formation processes. It is generally agreed that W4 was the first of the three large H II regions to be formed and that its expansion triggered collapse in at least part of the W3 molecular cloud (Dickel 1980; Thronson, Lada, & Hewagama 1985). Dickel derived an evolutionary model of the W3 complex based on molecular observations, as did Thronson et al. As early as 1954, it was speculated that W5 was physically related to W4 (Sajn 1954). However, Braunsfurth (1983) pointed out that formation of the stars in OCl 364, which excite W5, cannot have been triggered by W4 because they are too distant and only slightly younger than those in W4. The SNR HB 3 (G132.6+1.5), to the west of W3, is a shell-type remnant that has sometimes been thought to be interacting with this H II region (e.g., Caswell 1967) or with the molecular material associated with W3 (Routledge et al. 1991) and may have triggered cloud collapse and star formation.

While the W3/W4/W5/HB 3 region has frequently been studied, previous observations do not provide the combination of spatial coverage and resolution offered by a mosaic of DRAO synthesis fields. In particular, the best previous H I study of this complex (Braunsfurth 1983) had a spatial resolution of only 10′. This paper presents the data from the DRAO survey's pilot project. The observations are described in detail in § 2, and the data processing is covered in § 3. The continuum emission from the Galactic complex is described in § 4, and the neutral hydrogen distribution is discussed in § 5.

2. OBSERVATIONS

2.1. *Synthesis Telescope Observations*

DRAO's main instrument is a synthesis telescope operating simultaneously at 408 and 1420 MHz in continuum mode and at 1420 MHz in spectral line mode (H I). The main instrumental parameters are summarized in Table 1, and field center coordinates for these data are listed in Table 2. All observational parameters are described in more detail below.

The synthesis telescope (ST) consists of seven 9 m antennas placed along an east-west track. Four are fixed, and the other three are repositioned 11 times during observations while remaining at the same relative distance from

TABLE 1

OBSERVATIONAL PARAMETERS FOR THE SYNTHESIS TELESCOPE DATA

Parameter	Value
Bandwidth (MHz):	
408 MHz	4
1420 MHz continuum	30
1420 MHz spectral line	1
Primary beam FWHM (arcmin):	
408 MHz	305.5
1420 MHz	103
Polarization:	
408 MHz	RR
1420 MHz continuum	RR, LL, RL, LR
1420 MHz spectral line	RR
Calibrators:	
408 MHz	3C 147 (48.0 Jy), 3C 295 (54.0 Jy)
1420 MHz	3C 147 (22.0 Jy), 3C 295 (22.1 Jy), 3C 286 (14.7 Jy)
Center coordinates:	
Galactic (deg^2)	(134.76, 1.2)
J2000 (α, δ)	(2 33 56.08, 61 42 42.6)
Spatial coverage (deg^2, $l \times b$):	
408 MHz	$\sim 14 \times \sim 10$
1420 MHz	$\sim 8 \times \sim 6$
Spatial resolution (arcmin^2, EW $\times$ NS):	
408 MHz	3.5×4.0
1420 MHz	1.00×1.14
Central velocity with respect to the LSR (km s^{-1})	-50.0
Velocity coverage (km s^{-1})	211
Channel width (km s^{-1})	2.64
Channel separation (km s^{-1})	1.649
Sensitivity over the mosaic (theoretical):	
408 MHz (mJy beam^{-1})	1.9–16.5
1420 MHz continuum (mJy beam^{-1})	0.23–1.15
1420 MHz spectral line (K)	3.0–15.0

NOTE.—Units of right ascension are hours, minutes, and seconds, and units of declination are degrees, arcminutes, and arcseconds.

each other. There are therefore 21 baselines observed in every configuration, but nine of them are observed each time. All antenna spacings from a minimum of 12.86 m to a maximum of 604.29 m in steps of 4.29 m are observed, as well as 617.76 m for the continuum. The maximum spacing corresponds to a resolution of $1.0 \times (1.0 \csc \delta)$ arcmin^2 at 1420 MHz and $3.5 \times (3.5 \csc \delta)$ arcmin^2 at 408 MHz. The small baseline increment places the first grating ring well away from map center for a single field, its east-west radius being 2°.8 at 1420 MHz and 9°.8 at 408 MHz.

At 408 MHz, the ST's observing bandwidth is 4 MHz. In continuum mode at 1420 MHz, the total bandwidth is 35 MHz, divided into four 7.5 MHz–wide bands, two on either side of a central 5 MHz gap. The gap avoids contamination of the continuum emission data by Galactic H I spectral line emission, and the narrow bands reduce decorrelation of the signal within the field of view (bandwidth smearing).

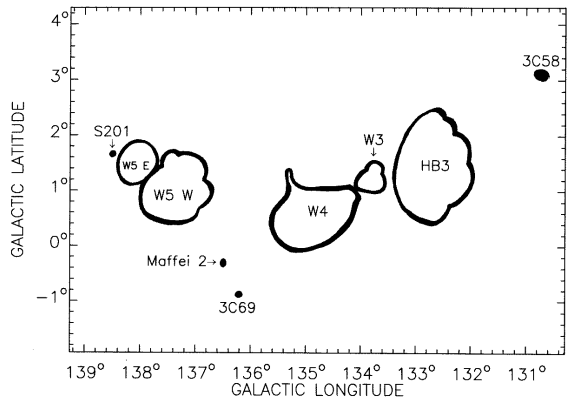

FIG. 1.—Sketch of the W3/W4/W5/HB 3 region. The main regions of continuum emission in the Perseus arm are outlined, and the Sharpless H II region S201 is indicated. Three other strong sources—3C 58, 3C 69, and Maffei 2—that are not in the Perseus arm are also indicated.

At the time of these observations, in 1993, the DRAO ST was equipped with 128-channel spectrometers for observations of the H I 21 cm spectral line. For the observations presented here, the total bandwidth was 1 MHz, which corresponds to a total velocity span of 211 km s^{-1}, centered at -50 km s^{-1} with respect to the local standard of rest (LSR). All velocities quoted in this paper are with respect to the LSR. The channel separation was 1.649 km s^{-1}, and the channel width was 2.64 km s^{-1}. Spectrometers are only

TABLE 2

FIELD NAMES AND POINTING CENTERS

Field Name	l (deg)	b (deg)	R.A. (J2000)	decl. (J2000)
HW	131.59	+1.20	2 08 18.66	62 47 17.3
HX	132.64	−0.63	2 12 08.56	60 43 39.2
HY	132.64	+3.03	2 22 27.06	64 11 20.1
HZ	133.70	+1.20	2 25 34.25	62 06 14.3
IA	134.76	−0.63	2 28 18.03	60 00 54.3
IB	134.76	+3.03	2 40 13.30	63 23 32.9
IC	135.81	+1.20	2 42 00.35	61 17 35.5
ID	136.87	−0.63	2 43 38.89	59 11 17.6
IE	136.87	+3.03	2 56 53.86	62 28 27.0
IF	137.92	+1.20	2 57 33.67	60 21 58.3

NOTE.—Units of right ascension are hours, minutes, and seconds, and units of declination are degrees, arcminutes, and arcseconds.

used on baselines combining one fixed with one movable antenna (12 baselines per configuration). Only redundancy is lost; no gaps are created in the visibility plane.

The flux density calibration scale follows that of Baars et al. (1977). The calibrators for these observations were 3C 147, 3C 295, and 3C 286. Their assumed flux densities are listed in Table 1. For the ST spectral line data, the overall gain, i.e., the gain over the whole band, is calibrated using these same sources. The calibration of the relative spectral channel gains (bandpass calibration) is done by using an artificial noise source.

In order to cover the entire W3/W4/W5/HB 3 region, 10 fields were observed. A lower limit for the range of possible field separations was determined from the confusion limit, and an upper limit was determined by the detectability of the dissociation and ionization regions around a B3 star in a typical interstellar medium (ISM) environment at the distance of W3. The resulting range was 72′–129′. To maximize area coverage, a field center separation near the upper limit was chosen, specifically, 126′. The sensitivity varies over the mosaic; the maximum values quoted in Table 1 correspond to the edges of the mosaic, where only one field contributes and the data points are far from the center of that field, so they are not typical of the sensitivity in the central part of the mosaic. Field centers (Table 2) were adjusted in such a way that the position of W3's peak flux was at the center of a field (HZ), in hopes of lessening associated artifacts. Four fields (HW, HX, HY, HZ) were observed in 1993 June and July. The remaining six were observed in November and December of that same year.

2.2. *Single-Dish Observations*

Because the individual antennas of the DRAO ST are never separated by less than 12.86 m, there is information missing that corresponds to large angular scale structure on the sky (greater than $\sim 3°$ at 408 MHz and greater than $\sim 1°$ at 1420 MHz). To compensate for this, data from large single-dish telescopes are used to fill in the gap in the visibility plane. In the case of the H I, the complementary data were observed by using the DRAO 26 m telescope. For the continuum, data were taken from published single-dish surveys (see § 3).

The 26 m telescope was used in frequency-switching mode to observe the large angular scale H I structure over the entire region. The FWHM of this telescope's beam is 36′. The spectrometers on the single dish were identical to those on the ST. The observations were made on a 64×48 grid with a 16′ spacing, or slightly less than $\frac{1}{2}$ beamwidth. Calibration was done directly in brightness temperature, using the standard region S7 ($T_b = 100$ K; Williams 1973). There was however a slight mispointing during calibration. When adding these low-resolution data to the ST data, a correction factor was applied to compensate for this error. The correction was $\sim 3\%$, and an error in this factor could only be slight and would not noticeably affect the images.

3. DATA PROCESSING

3.1. *Continuum Emission Data*

Data at both continuum frequencies were processed in a similar fashion. The raw visibilities were edited to eliminate interference and the effects of obvious instrumental failures. An automatic routine eliminated prominent interference spikes, after which the data were examined and further editing was done manually. Calibration corrections were then applied by using an average of the pre- and postobservation calibrator data. The calibration observations closest in time to the field observation were used, with at most an interval of 1 day being permitted. On a few occasions, only one suitable calibrator was available because of such things as solar interference or antenna phase jumps. However, this does not affect the quality of the data: the array is quite stable—analysis showed that observing calibrators every 2 days would be sufficient—and the data are later self-calibrated in any event.

Once calibrated, the visibilities were gridded and then Fourier transformed into the image plane. At 408 MHz, only right-circular data were taken, but at 1420 MHz both right- and left-circular polarizations were observed, and therefore Stokes I maps could be produced. Cross-polarization data were also collected, and so other Stokes parameters—and therefore polarization angle and intensity—can be imaged; these data will be discussed elsewhere (Gray et al. 1996). The CLEAN algorithm (Clark 1980; Steer, Dewdney, & Ito 1984) was used to deconvolve the instrumental response function from the data, thereby eliminating the sidelobes from the images. Atmospheric and residual instrumental phase and amplitude errors were eliminated, or at least reduced, by using self-calibration. This improved image quality considerably and was essential for imaging the W3 region. The data were self-calibrated until there was no longer any noticeable improvement. This is admittedly subjective, and further improvements to the images may have been possible. The number of iterations varied from field to field, depending on the emission present. For example, for field IF, in which there are no bright features and therefore no strong sidelobes, only one iteration was required whereas, for HZ, 10 iterations were required because of the presence of W3 and its associated artifacts. Once the "final" self-calibrated ST image was obtained, it was corrected for the primary beam of the telescope. At both frequencies this was approximated as a Gaussian, with an FWHM of 305′.5 at 408 MHz and 103′ at 1420 MHz. The primary beams of the DRAO ST have recently been re-evaluated, and the results of these measurements will be used for the processing of the data from the full survey.

As mentioned previously (§ 2.2), low spatial frequencies are missing from the ST data, and it is standard practice at DRAO to fill the gap by using data from large single-dish surveys. At 408 MHz, these were obtained from the Haslam et al. (1982) all-sky survey. For the 1420 MHz continuum, they were provided by the Effelsberg survey (Kallas & Reich 1980) and the Stockert survey (Reich 1982). The Effelsberg survey was used whenever possible, but as it only extends up to $+4°$ in latitude, it was necessary to use the Stockert survey at higher latitudes. The missing large-scale information was added on a field-by-field basis, and as a result only the three higher latitude fields contain a mixture of Stockert and Effelsberg data. Both the ST and single-dish data sets were spatially filtered, with inverse gradual transitions between zero and full weight in the overlap region of the visibility plane, before being added together. At 408 MHz, an automatic level control (ALC) system keeps the receiver output constant, i.e., the total signal (cosmic signal plus system noise) is held constant. This means that the gain can vary substantially between observations of the calibrator source, which is far removed from the Galactic plane, and the observed field. For example, for field IC, the gain varied

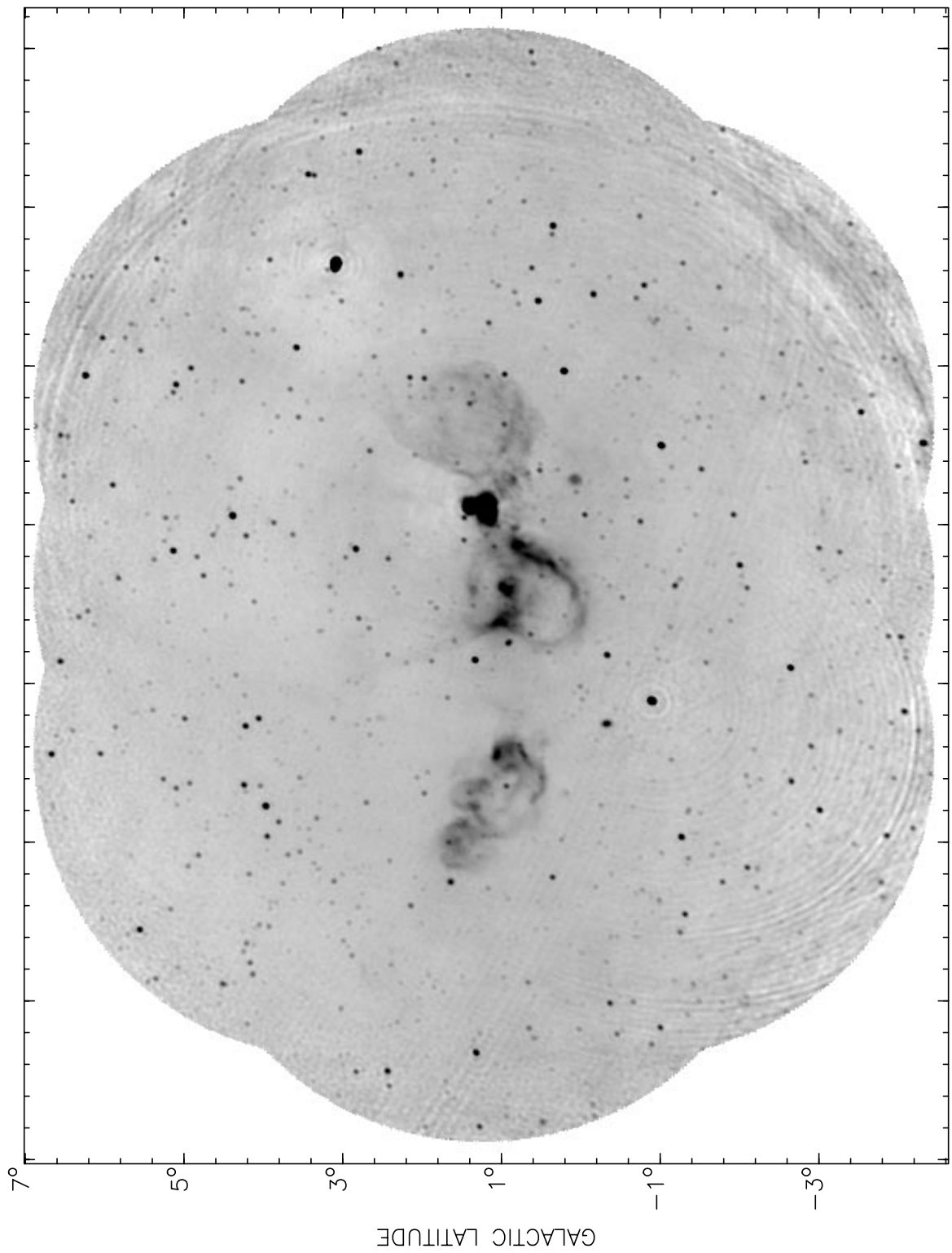

FIG. 2.—The 408 MHz continuum mosaic. All emission below 10 K is in white, and that above 200 K is in black. The actual image maximum is 3193 K. As a result, the internal structure of the very bright W3 H II region, centered at (133°.7, 1°.2), is not apparent. West of W3, one can see the HB 3 SNR, and to the east is the W4 H II region. At still higher longitudes is the W5 H II region. The bright compact source at (130°.7, 3°.1) is the SNR 3C 58. Ring artifacts associated with 3C 69 (136°.21, −0°.9) remain, as well as large-radius rings centered on W3. In both cases these artifacts are most apparent toward the edges of the mosaic, where only one field contributes to the overall image. The faint striping that diagonally traverses the lower half of the mosaic is attributable to man-made sources of interference. The resolution of this image is ~3'.5.

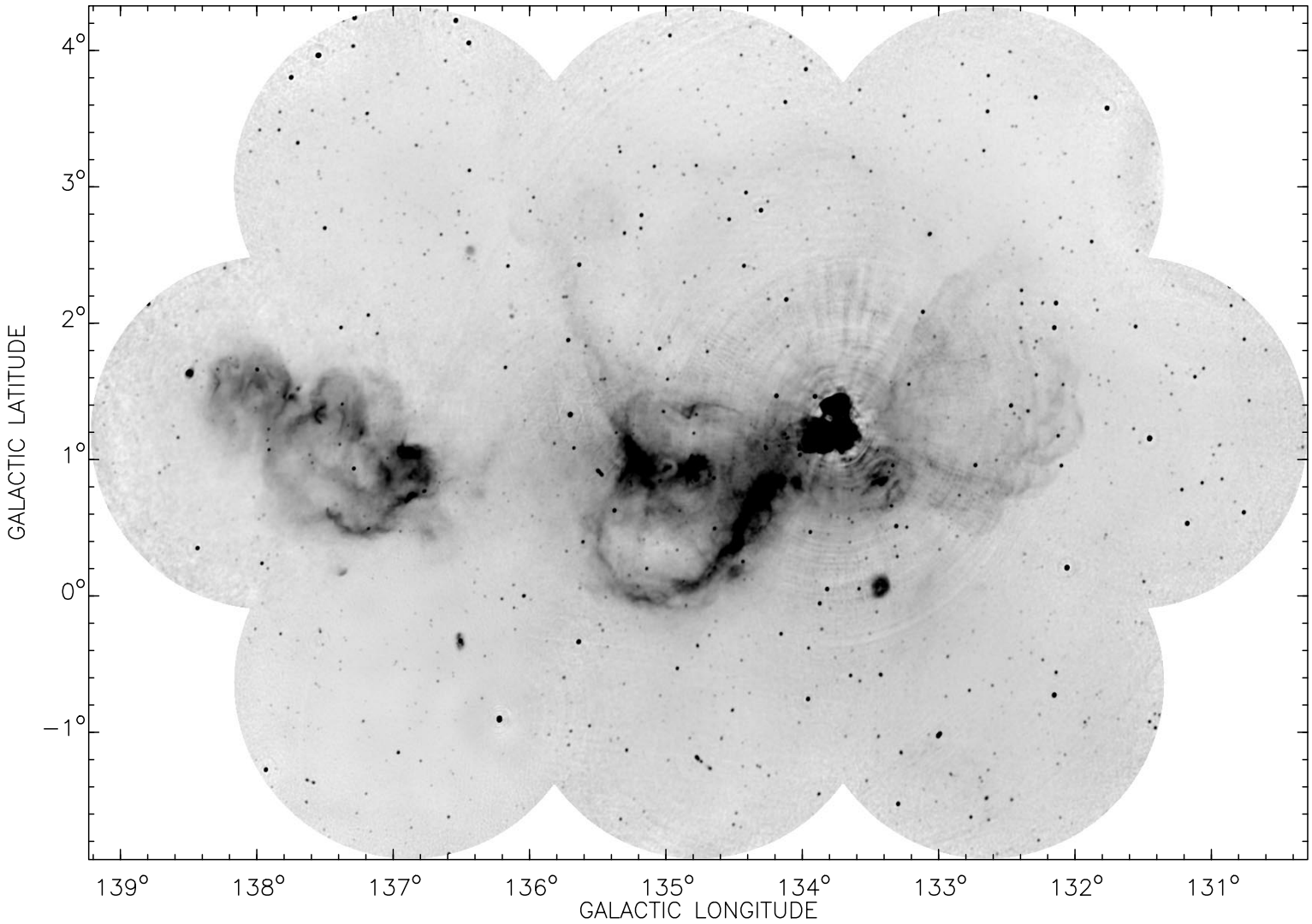

FIG. 3.—The 1420 MHz continuum mosaic. All emission below 0 K is in white, and that above 10 K is in black. This image is supersaturated, the actual maximum being at 2166 K. Again, the internal structure of W3 is not apparent. The scalloped appearance of SNR HB 3 is more apparent on this image than at 408 MHz (Fig. 2), as are the internal structures of both W4 and W5. In the vicinity of W3, the image is marred by artifacts associated with W3. The resolution is $\sim 1'$.

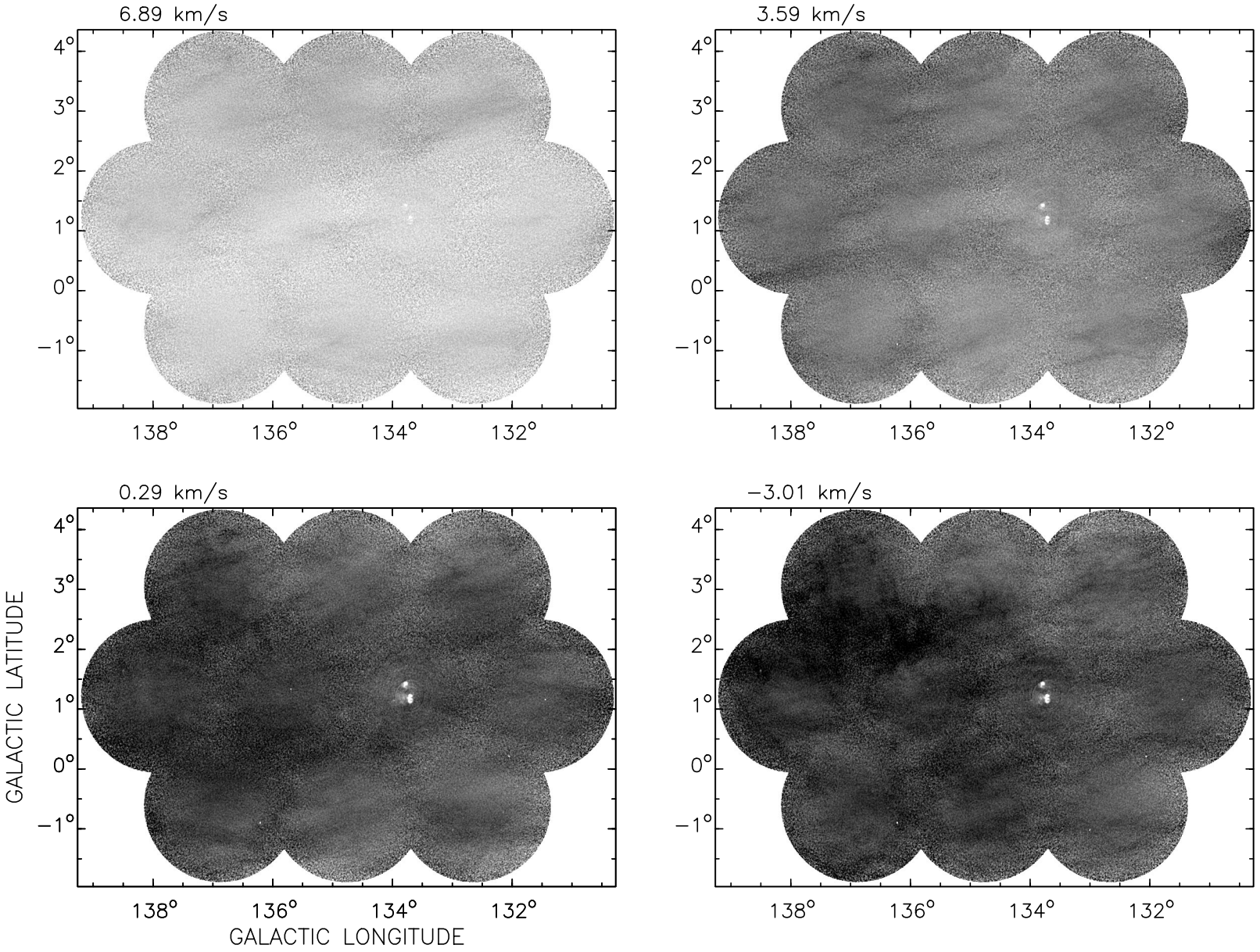

FIG. 4*a*

FIG. 4.—The H I mosaics. The images presented here are averages of two adjacent spectral channels. Only the $+7$ to -107 km s^{-1} interval is shown, other velocity channels being essentially devoid of H I. Image intensities below 0 K are in white, i.e., all absorption is in white. The maximum of the gray-scale representation varies but is constant for each group of four images. It is 50 K for (*i*), 80 K for (*a*)–(*c*) and (*g*)–(*h*), and 100 K for (*d*)–(*f*). The interested reader is referred to the Web site (see text) for higher dynamic range and higher velocity resolution representations of the H I data.

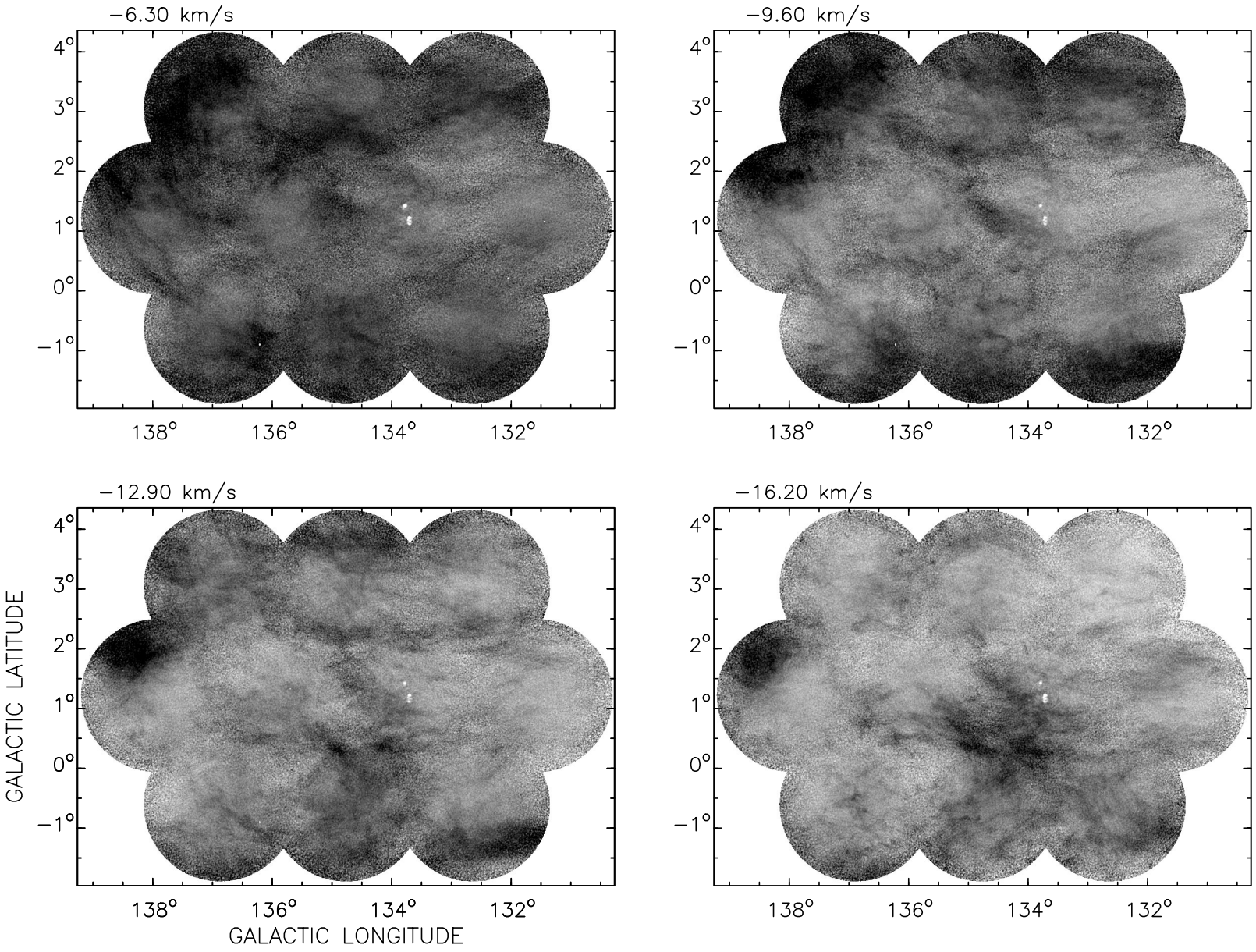
−6.30 km/s
−9.60 km/s
−12.90 km/s
−16.20 km/s
4°
3°
2°
1°
0°
−1°
138°
136°
134°
132°
GALACTIC LATITUDE
GALACTIC LONGITUDE

FIG. 4*b*

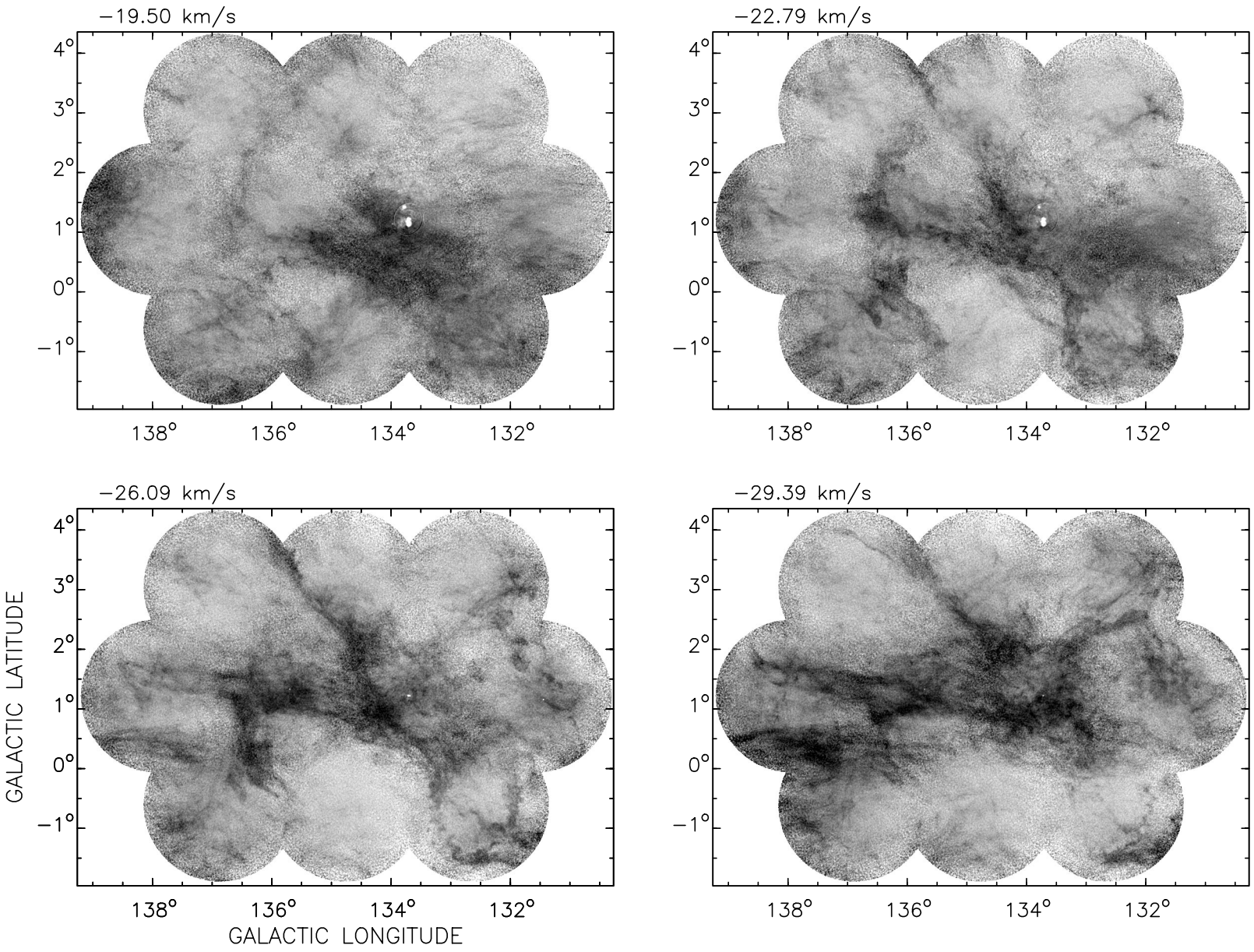
−19.50 km/s
−22.79 km/s
−26.09 km/s
−29.39 km/s
4°
3°
2°
1°
0°
−1°
138°
136°
134°
132°
GALACTIC LATITUDE
GALACTIC LONGITUDE

FIG. 4c

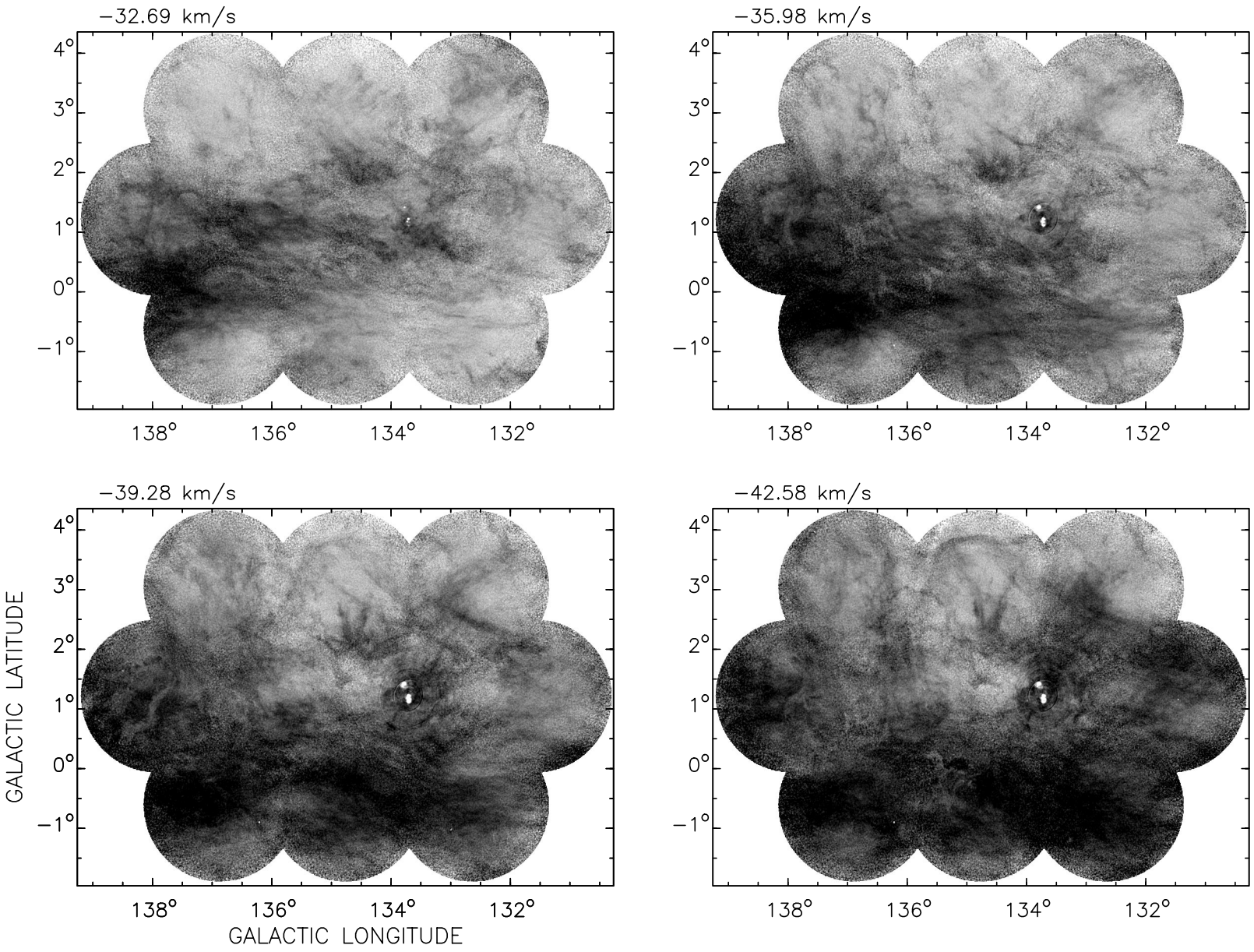
−32.69 km/s
−35.98 km/s
−39.28 km/s
−42.58 km/s
4°
3°
2°
1°
0°
−1°
138°
136°
134°
132°
GALACTIC LATITUDE
GALACTIC LONGITUDE

FIG. 4*d*

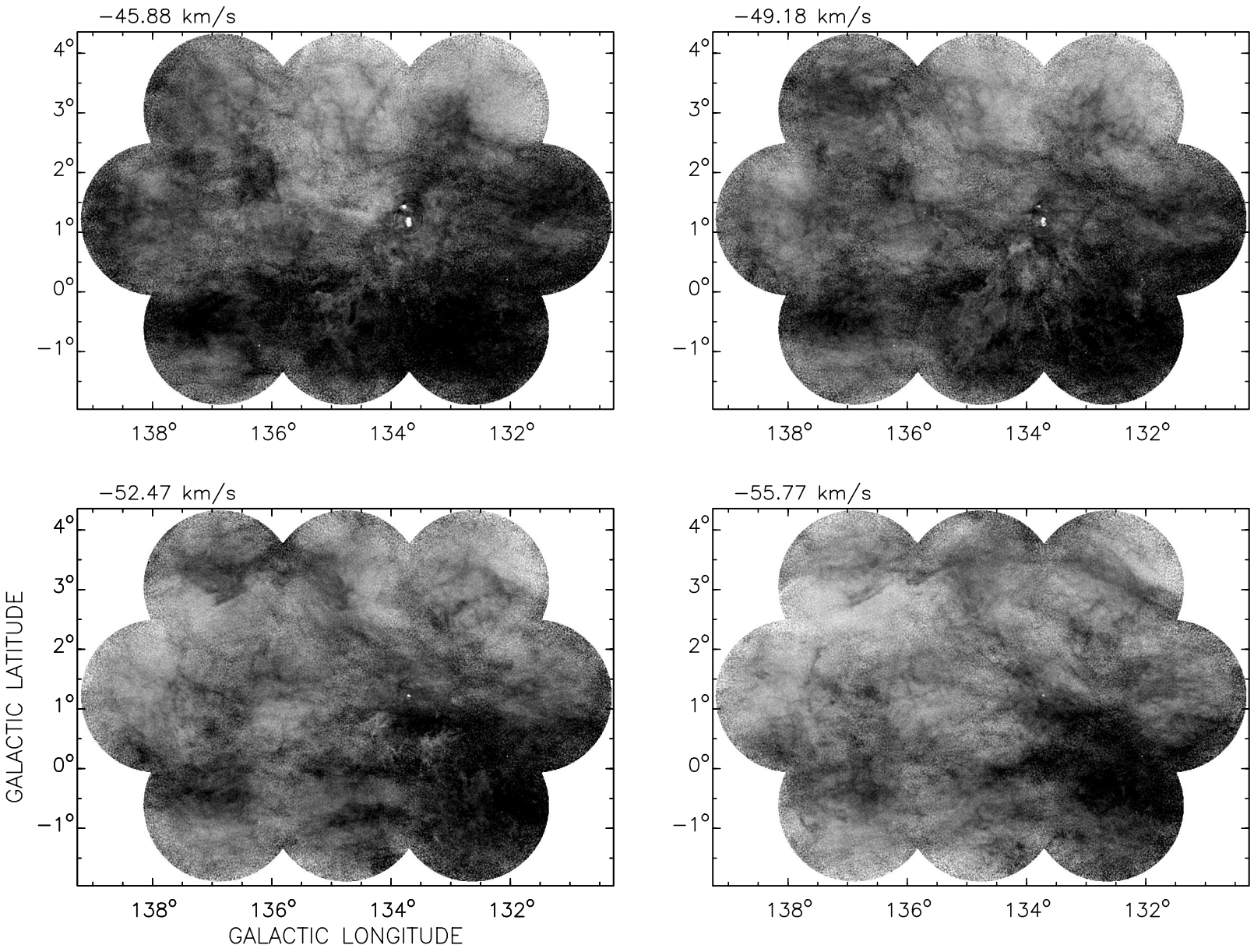
−45.88 km/s
−49.18 km/s
−52.47 km/s
−55.77 km/s
4°
3°
2°
1°
0°
−1°
138°
136°
134°
132°
GALACTIC LATITUDE
GALACTIC LONGITUDE

FIG. 4*e*

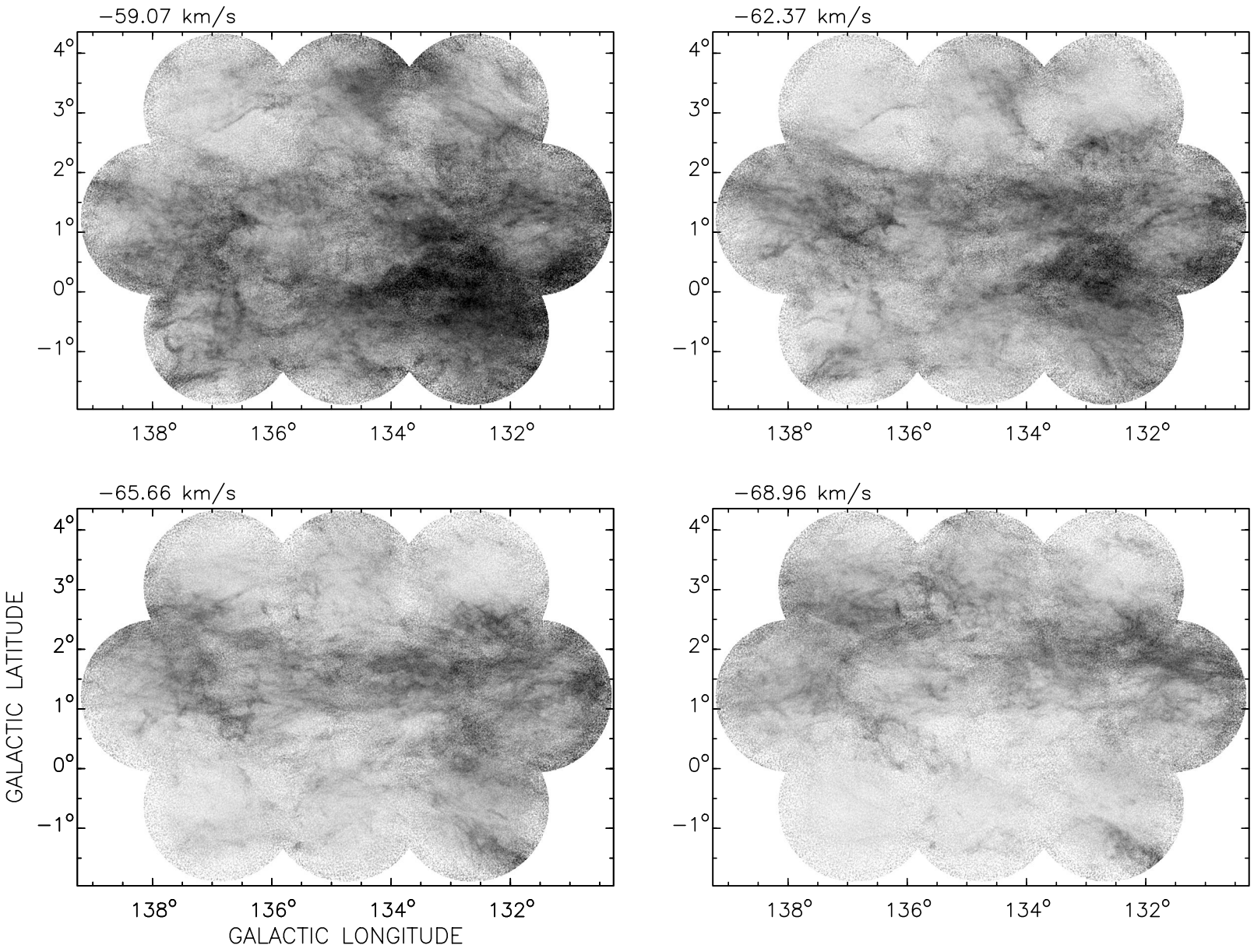
−59.07 km/s
−62.37 km/s
−65.66 km/s
−68.96 km/s
4°
3°
2°
1°
0°
−1°
138°
136°
134°
132°
GALACTIC LATITUDE
GALACTIC LONGITUDE

FIG. 4*f*

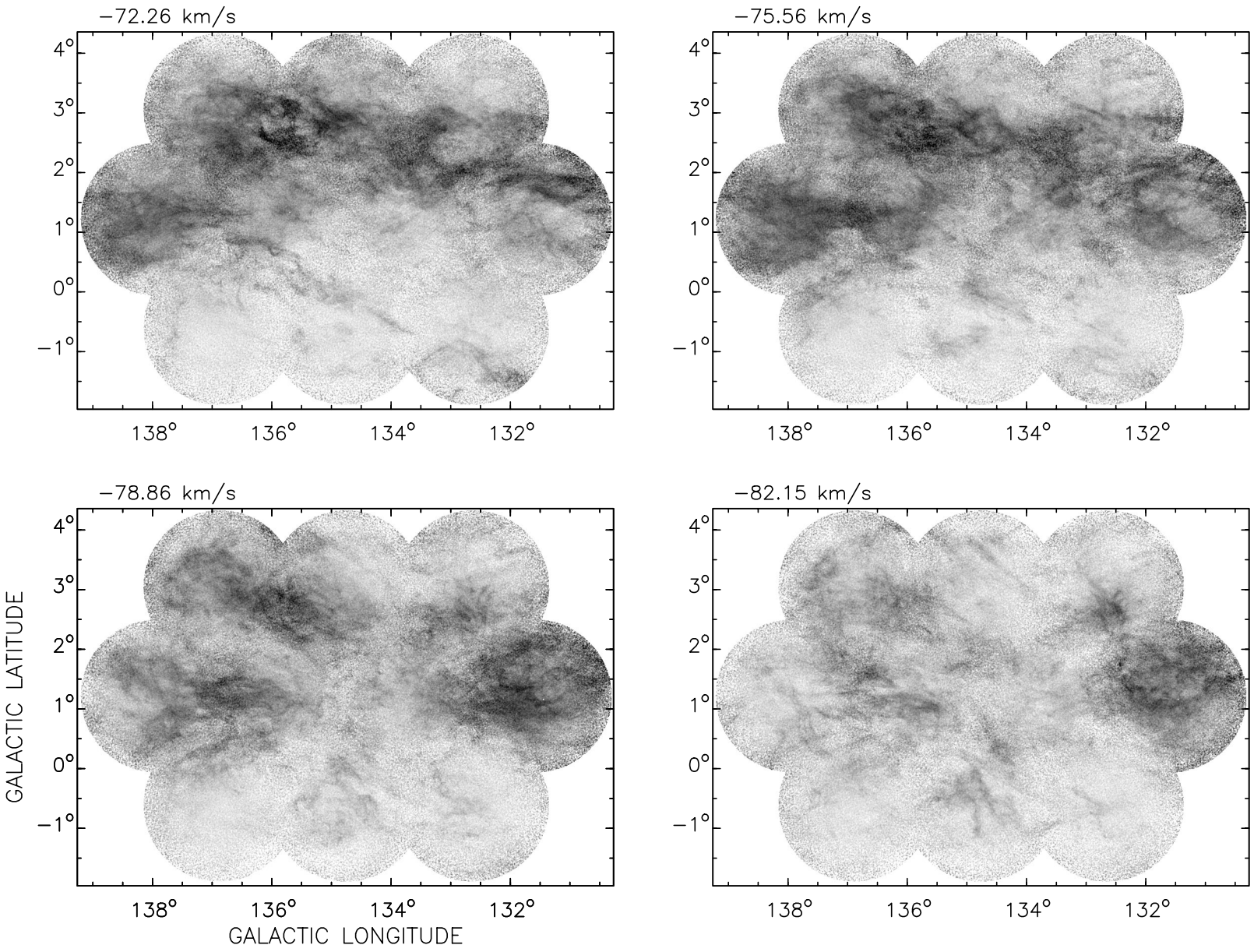
−72.26 km/s
−75.56 km/s
−78.86 km/s
−82.15 km/s
4°
3°
2°
1°
0°
−1°
138°
136°
134°
132°
GALACTIC LATITUDE
GALACTIC LONGITUDE

FIG. 4*g*

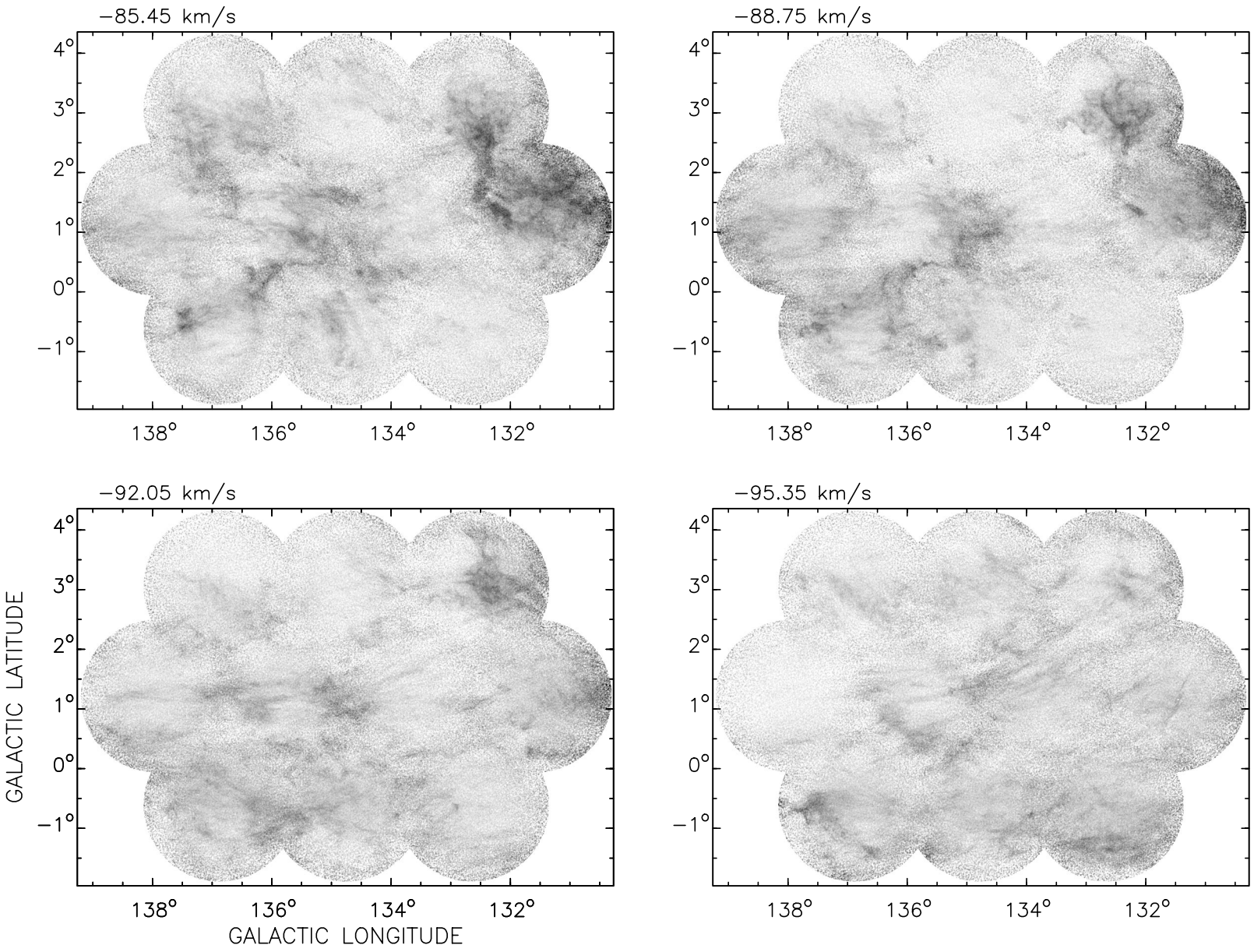
−85.45 km/s
−88.75 km/s
−92.05 km/s
−95.35 km/s
4°
3°
2°
1°
0°
−1°
138°
136°
134°
132°
GALACTIC LATITUDE
GALACTIC LONGITUDE

FIG. 4*h*

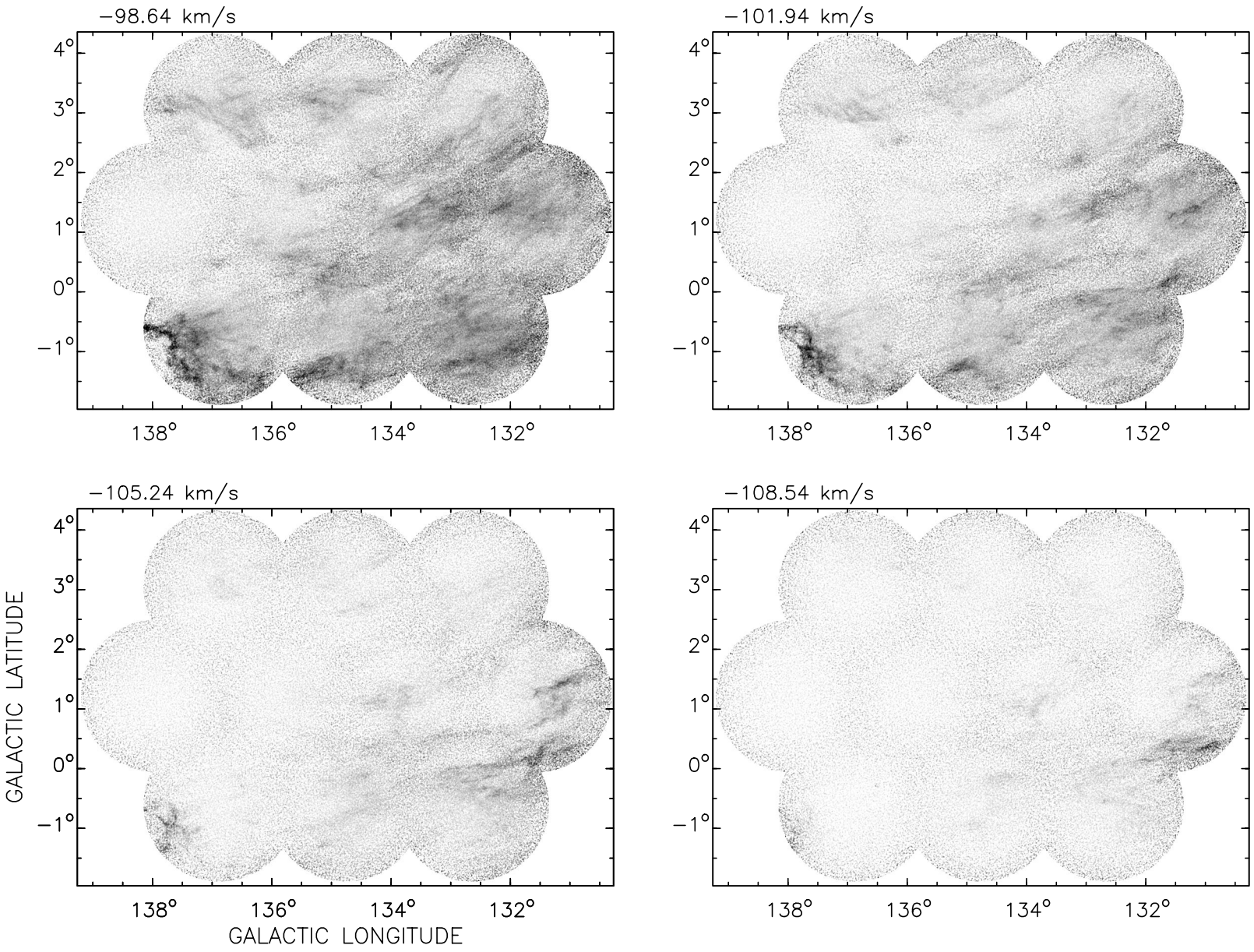
−98.64 km/s
−101.94 km/s
−105.24 km/s
−108.54 km/s
4°
3°
2°
1°
0°
−1°
138°
136°
134°
132°
GALACTIC LATITUDE
GALACTIC LONGITUDE

FIG. 4*i*

by a factor of 1.19 between calibrator and observation fields. When merging the high- and low-resolution data, a correction factor was applied to compensate for the ALC.

Once all fields had full visibility coverage images, a mosaic was created. The contribution of the individual fields was restricted to the region within which the sensitivity was greater than 20% (232.8 for the 408 MHz primary beam and 78′ for the 1420 MHz primary beam). The weight attributed to a given field varies with distance from its center, according to the sensitivity of the primary beam. The 408 MHz continuum image is presented in Figure 2, and the 1420 MHz data are shown in Figure 3. Some artifacts are still noticeable in these images, particularly around W3 at 1420 MHz. At this frequency, W3 has a peak flux density of 14 Jy, and therefore any residual artifacts (e.g., sidelobes, grating rings, and "spokes," which are an artifact of processing for strong, difficult-to-model sources) will be quite noticeable around such a strong source (fluctuations on the order of 3.0–4.5 mJy beam^{-1}). Residual rings can also be seen around 3C 69 ($l = 136.^\circ21$, $b = -0.^\circ90$) and 3C 58 ($l = 130.^\circ72$, $b = +3.^\circ08$).

3.2. *Spectral Line Data*

The spectral line visibilities were edited to eliminate interference and the effects of instrumental problems. They were then transformed into the image plane, creating a set of constant-velocity maps for each observed field.

The continuum emission was subtracted from the spectrometer data. To do so, a pseudocontinuum image was created using the outer channels, which are devoid of Galactic H I emission, and this was subtracted from each constant-velocity map. For one of the 10 fields, this procedure could not be followed; in field ID, the starburst galaxy Maffei 2 (S197) has associated H I structure in the extreme velocity channels. Therefore the 1420 MHz continuum image was used after appropriately scaling to account for the effect of the ALC affecting the spectral line system. Because of the nature of the spectral line images, i.e., dominated by diffuse structure for which the residual sidelobe level is generally below the noise level, they were not CLEANed, with the exception of field HZ. This field was CLEANed before subtracting the continuum, in an effort to reduce the artifacts related to the strong continuum absorption from W3. After subtraction of the continuum, the data were corrected for the primary beam of the telescope.

Low-resolution images from the 26 m telescope were added to the ST data on a field-by-field basis. At this stage, the correction factor for the calibration mispointing of the 26 m was applied, as well as an ALC correction for the ST. Once all fields had full spatial coverage maps at all velocities, mosaic images were created in the same fashion as for the continuum. The resulting constant-velocity images are presented in Figure 4 for the $+7$ to -107 km s^{-1} interval, other channels being essentially devoid of H I emission. The images presented here are averages of two adjacent channels. The full data cube can be viewed at ⟨http://www.ras.ucalgary.ca/pilot_project.html⟩. The effect of increased noise at the edges of individual fields can be seen on the images, particularly at velocities at which the sky has a more or less uniform brightness.

4. RADIO CONTINUUM EMISSION

The radio continuum emission is dominated by the star formation activity in the Perseus arm. The young, massive stars of this region greatly affect the surrounding ISM, creating ionization regions as well as engendering shock fronts and blowing bubbles. In-depth analysis of individual features is beyond the scope of this paper; however, an overview of the main constituents of the Galactic complex is presented here.

4.1. *The W3 Region*

The small-scale structure of W3 has been studied repeatedly (e.g., Roelfsema & Goss 1991; Oldham et al. 1994). It is the youngest of the three H II regions and a region of active star formation—there are several masers, and 59 of Elmegreen's (1980) 135 bright infrared stars (BIRSs) in the W3/W4 area are within 0.°3 of the center of W3 in projection.

Figure 5 shows the W3 area with the contrast adjusted to highlight the structure of this region. At the resolution of the data presented here, it can be subdivided into three main components: the very compact northern component, W3 N, centered at ($133.^\circ78$, $1.^\circ43$); W3 W, centered at ($133.^\circ71$, $1.^\circ16$); and the more diffuse W3 E, centered at ($133.^\circ86$, $1.^\circ19$) with an extent of $\sim 0.^\circ25$. The combination of W3 W and W3 E is sometimes referred to as W3(main). W3 N has an integrated flux density of 18 ± 2 Jy at 408 MHz and 26.4 ± 0.3 Jy at 1420 MHz, giving it a spectral index of $+0.3$. As for W3(main), a spectral index of $+0.2$ is obtained from flux densities of 62 ± 8 Jy at 408 MHz and 76.6 ± 0.8 Jy at 1420 MHz. Twisted-plane backgrounds fitted to the edges of polygons surrounding the sources were subtracted when the fluxes were integrated. The uncertainties reflect the scatter of the integration results.

Because of the variety of observations that have been carried out for the W3 region, the nomenclature has understandably become somewhat confusing, and the reader is referred to Table 4 of Dickel et al. (1980) for a summary. The following presents some of the main coincidences but is by no means exhaustive.

The northern component, W3 N or G133.8+1.4, is an H II region that, according to Ogura & Ishida (1976), is ionized by an O8 star (No. 102 of their list). There are four BIRSs within 1′ of the stated central position. Further, Brand et al. (1994) associated water maser emission with IRAS 02230+6202, which is also positionally coincident with W3 N and no doubt engulfs the four BIRSs.

Within the region defined for W3 E, there is an O8 star (BD $+61^\circ411$) that Garmany & Stencel (1992) considered to be part of the Cas OB6 association and an O7 star identified by Ogura & Ishida (No. 109). Both are toward the eastern edge of the region. Because of their position, these stars cannot suffice to ionize this entire region. As for infrared sources, there are four BIRSs and four compact sources cataloged by *IRAS* that may or may not be distinct from the BIRSs. There is also a maser, GAL 133.75+01.20, which, according to Palagi et al. (1993), is not associated with an *IRAS* compact source, though they did point out that this does not necessarily mean that there is no associated far-infrared emission.

As for W3 W, it can be further subdivided into a very bright, unresolved double source at ($133.^\circ72$, $1.^\circ22$) and, below it, a fainter ring of emission with three bright compact sources on its periphery at ($133.^\circ70$, $1.^\circ17$), ($133.^\circ72$, $1.^\circ12$), and ($133.^\circ73$, $1.^\circ18$), the first two being truly on the ring and the third only slightly offset. What appears here as

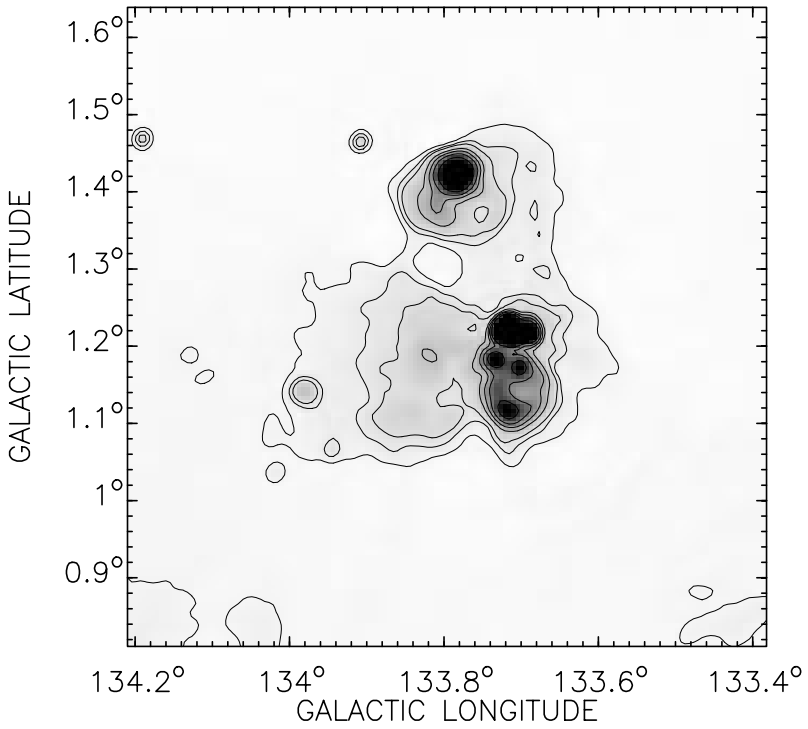

FIG. 5.—The W3 region at 1420 MHz. Contrasts have been adjusted to reveal the structure of the W3 area. The gray scale varies linearly between 0 and 250 K. Contours are at 10, 20, 30, 60, 90, 130, and 200 K. The compact source to the north is W3 N. The group of bright sources south of this constitute W3(main). The more diffuse, extended emission to the east is W3 E.

an unresolved double source coincides with the positions of W3A and W3B (Wynn-Williams, Becklin, & Neugebauer 1972). It corresponds to what Dickel et al. (1980) referred to as the northern group of W3(main) and, with better resolution, could be subdivided into at least five compact H II regions. There are five of Elmegreen's BIRSs within 1′ of the central position, as well as three masers. This is the least evolved region of the W3 complex (Dickel, Harten, & Gull 1983). The three sources around the ring to the south are compact H II regions. The two higher latitude ones are also known as radio sources K and J. There are BIRSs associated with each of these positions, seven in the case of the source just slightly off the ring (source K).

4.2. *The W4 Region*

The W4 region, adjacent to W3, is composed of a ridge of thermal emission at $l \sim 0\overset{\circ}{.}9$ and a large loop of ionized gas to the south. It is ionized by the open cluster OCl 352, which contains some 145 stars (Strobel 1992), nine of which are O type. The cluster is situated within the northern ridge, centered at ($134\overset{\circ}{.}74$, $0\overset{\circ}{.}92$).

Surrounding W3/W4 and HB 3 there is a faint, extended halo that was noted by Braunsfurth (1983) in the Effelsberg 21 cm continuum survey data. It extends to the north and south of W4 and southeast of HB 3.

Because of the presence of the Galactic nonthermal background emission, such a faint halo is not discernible in our 408 MHz data. At 1420 MHz, it appears at a level of 2–3 K. It is quite apparent in the Effelsberg 2695 MHz (11 cm) Galactic plane survey (Fürst et al. 1990), in which it is at a comparable level, indicating that it has a flat spectrum and is most likely a thermal emission structure.

This structure can be subdivided into two separate components: one northward of W4 and the other comprising the ionized gas to the south of HB 3 and W4. The faint continuum emission north of W4 is most likely linked to the chimney phenomenon proposed for this region (Normandeau, Taylor, & Dewdney 1996), with the OCl 352 cluster stars providing the ionizing radiation. As for the southern region, two main explanations suggest themselves with respect to its nature. First, it may be an old, background, low-density H II region, a remnant from a previous epoch of star formation. The second possibility is that this halo is formed by ionizing radiation escaping from W4 and is therefore a product of the present generation of stars.

4.3. *The W5 Region*

The third large H II region, W5, does not seem to be interacting with the other two, although there is a "bridge" of faint continuum emission between it and W4. It can be divided into two main components: an eastern, spherical shell (W5 E) with a diameter of $\sim 0\overset{\circ}{.}7$, and a western, more extended and amorphous region (W5 W). The western section is excited by the open cluster OCl 364, which contains four O-type stars. In the eastern shell, there is only one O-type star visible, BD $+59°578$.

There is no detectable extended continuum halo around the W5 region. If one assumes that the halo around W4 is produced by radiation leakage, why is there no corresponding structure around W5? It is, after all, only slightly younger and is evolving in a similarly composed ambient medium. Perhaps the explanation lies in the clumpiness of W4, which would allow ionizing radiation to leak out, whereas W5 better confines radiation, i.e., it is ionization

bounded. It should be noted as well that the OCl 364 cluster is not as rich as OCl 352 and therefore produces fewer high-energy photons.

4.4. *The SNR HB 3*

The last major continuum-emitting member of the complex is the evolved supernova remnant HB 3. Centered at (132°.6, 1°.5), this shell-type SNR has dimensions of $93' \times 123'$ east-west by north-south. Based on indications of interaction with the W3 molecular cloud, a distance of 2.2 kpc has been assigned (Routledge et al. 1991), giving it spatial dimensions of approximately 60 pc × 79 pc.

Landecker et al. (1987) presented 408 MHz observations of this object taken with the DRAO ST. The present data are similar, though they have greater sensitivity, which reveals weaker emission features. The improvement in sensitivity is mainly due to the fact that the present image of HB 3 is made from seven overlapping fields. The 1420 MHz image of HB 3 constitutes the highest resolution radio continuum observation to date of this SNR. Although it is marred by artifacts associated with W3, it shows the scalloped structure of the SNR quite well. Fesen et al. (1995) discuss the radio continuum data from the pilot project and compare the structures seen at these frequencies with deep optical images of the remnant. They find a good correlation between the two frequency regimes. From a *T-T* plot (brightness temperature at 1420 MHz plotted against that at 408 MHz) of the pilot project data, they find a spectral index of -0.64 ± 0.01, in agreement with Landecker et al. (1987), who found -0.60 ± 0.04 from a fit to all flux densities published at the time.

5. ATOMIC HYDROGEN

The H I data cube contains a plethora of filaments, arcs, shells, bubbles, and ridges. In this section an overview of the global H I distribution is presented, and some of the salient features associated with the Galactic complex in the Perseus arm are pointed out.

5.1. *Global Distribution*

5.1.1. *Velocity-Longitude Plots*

Figure 6 presents the velocity distribution of the H I as a function of longitude. The top panel shows the velocity-longitude (*v-l*) plot for an average over all latitudes. It shows two distinct bands of emission, one between 0 and -10 km s^{-1}, which arises from emission in the Local spiral arm, and one from -30 to -70 km s^{-1} associated with the Perseus spiral arm. Between these two arms there is less intense H I emission; this interarm region is less clearly demarcated in atomic gas than it is in molecular data sets (see, e.g., Digel et al. 1996). The main ridge of emission of the Perseus arm is centered at -50 km s^{-1} or so at lower longitudes but gradually becomes closer in velocity, reaching approximately -40 km s^{-1} at the higher longitude end of the mosaic. Beyond the Perseus arm, there is no strong concentration of H I emission as clearly defined as the two aforementioned spiral arms. However, the H I does occur in bands, primarily concentrated in the -70 to -80 km s^{-1} interval, and, more weakly, in the -90 to -100 km s^{-1} range.

The reader is reminded at this point that the extreme longitudes of the mosaics are not present at all latitudes (see Fig. 4), and so, particularly for $l > 138°.2$ and $l < 131°.4$, which only contain contributions from the row of fields centered on $b = 1°.2$, the structures seen on the average plot are not necessarily typical of the general distribution of atomic gas. For instance, near $l = 139°$ the local gas distribution appears split, with a trough at -10 km s^{-1}; this may be typical only of the central latitudes.

Figure 6 also shows *v-l* plots for five individual latitudes: $+3°.0$, $+2°.0$, $+1°.0$, $0°.0$, and $-1°.0$. This illustrates the variations with latitude that prompted the warning in the previous paragraph. In particular, the Perseus arm is well defined for lower latitudes but much less so for $b > 0°$. At $b = +1°.0$, the Perseus H I is much broadened for longitudes between 133° and 136°.5. This corresponds to the position of W3/W4 and is likely attributable to the energetics of these H II regions. On the $b = +3°.0$ plot, there is a clear concentration of H I at $v \sim -70$ km s^{-1}, separated from the Perseus gas by a well-defined gap, at least at mid to higher latitudes, while, at lower latitudes, there is no such structure. The band of H I emission at -90 to -100 km s^{-1} is present at all latitudes; it most likely represents extended diffuse H I structures.

5.1.2. *Constant-Velocity* H I *Images*

The distribution of H I in the images of Figure 4 will now be discussed, beginning at positive velocities. At these longitudes, if all atomic hydrogen followed a monotonic Galactic rotation curve (i.e., circular motion), there should be no H I at positive velocities. Consequently, there is very little emission at these velocities; the average value is 4.4 K for all positive-velocity mosaics, and what few structures are present cannot be assigned a distance. However, the turbulent velocity of the ISM is typically ~ 8 km s^{-1}, and as a result low-velocity features are likely to be local gas. There is an interesting striation pattern at $v \sim +4.5$ km s^{-1}, mostly at higher *b*, which is not quite parallel to the plane.

At 0 km s^{-1}, there is bright, diffuse emission everywhere, corresponding to the bulk of the local H I, comprising broad bands that are elongated at a slight angle to the plane. Localized structure starts to appear as soon as the velocities become negative and is initially concentrated mostly in the higher longitude and latitude corner of the mosaic. Out to -10 km s^{-1} or so (Local arm), the gas is very diffuse and widespread.

The gas in the interarm region (-10 to -30 km s^{-1}) appears more highly structured on scales of several degrees, with filaments extending over a sizable fraction of the mosaic. Within this velocity interval, there is a large H I shell centered at $(l, b, v) = (132°.6, -0°.6, -25$ km $s^{-1})$. There is also a filament that diagonally traverses the mosaic, starting at the northeast edge of the shell and continuing through to $(136°.0, +3°.9)$ and, from there, off the edge of the mosaic. It is not clear whether this is one coherent structure. At velocities around -28 km s^{-1}, most of the H I is concentrated in the central part of the mosaic, overlapping the projected position of W3/W4.

As one moves toward more negative velocities, one enters the bulk of the Perseus arm's H I. There is a great deal of structure, some of which can be related to the features seen in the continuum. These will be described in more detail in § 5.2. The H I becomes sparser around -60 km s^{-1} and primarily occupies a band between $b = 1°$ and $b = 3°$, moving toward higher *b* as *v* increases.

By -83 km s^{-1}, there is very little H I left except at low longitudes and medium to high latitudes. What little H I

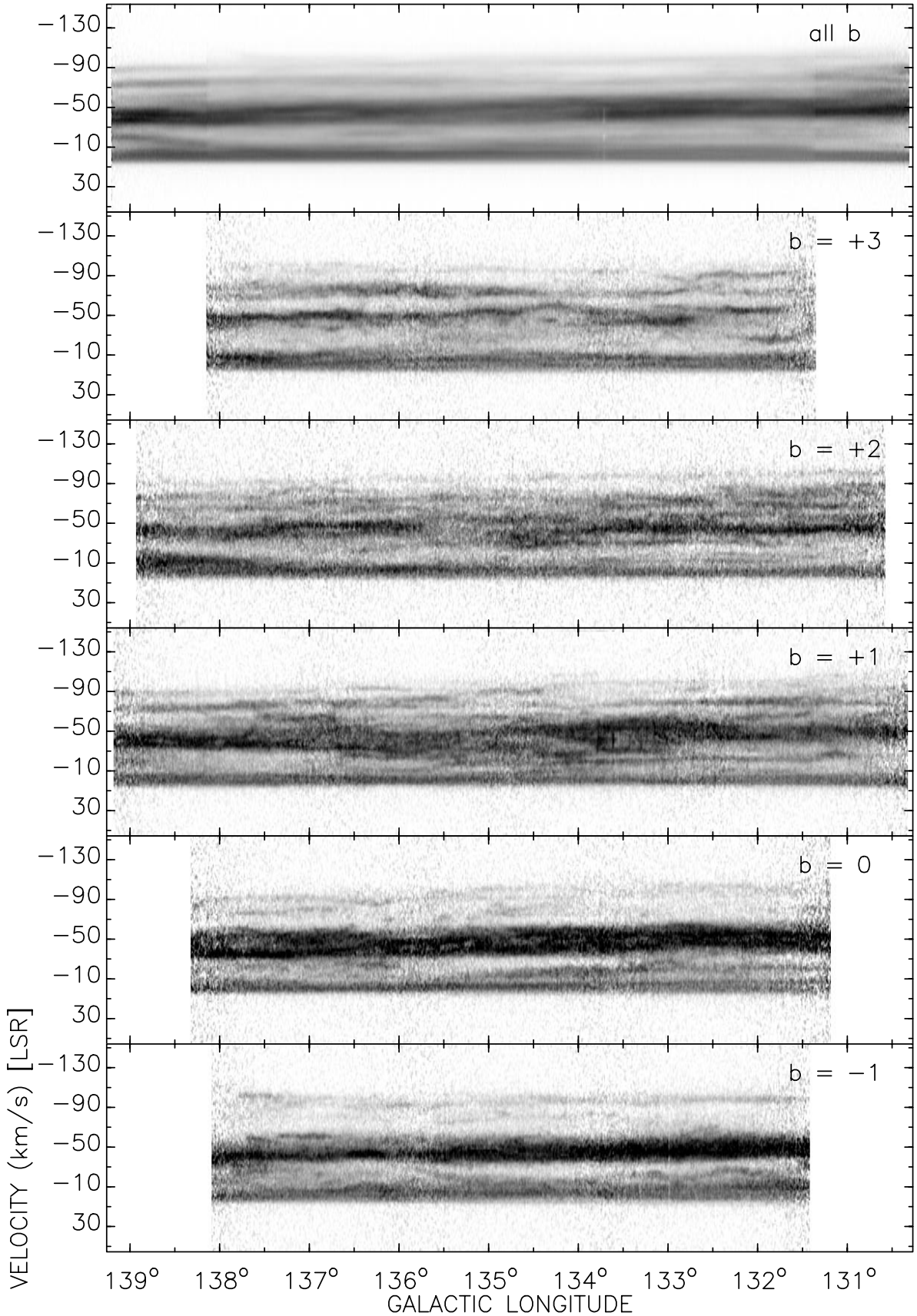

FIG. 6.—H I velocity-longitude plots. All absorption is in white, and the maximum of the gray scale is set at 80 K. The top panel is an average over all latitudes and thus represents the general distribution of atomic hydrogen. The following panels are, in order, for $b = +3\overset{\circ}{.}0$, $+2\overset{\circ}{.}0$, $+1\overset{\circ}{.}0$, $0\overset{\circ}{.}0$, and $-1\overset{\circ}{.}0$. These illustrate the variation of the H I distribution with latitude.

there is past -91 km s^{-1} is very wispy in appearance. Finally, at extreme negative velocities, from -96 to -101 km s^{-1}, there are intriguing aligned filaments. They seem to be slightly curved, with a center of curvature far above the Galactic plane and at higher longitudes.

It is important to keep in mind that assigning distances to H I assumes that the emitting gas follows the rotation curve, i.e., that it has not been accelerated by such phenomena as supernova events or stellar winds. Because of the intense activity in the Perseus arm, much of the H I may in fact be displaced, and so this walk-through in velocity does not necessarily correspond to a walk-through in distance.

5.1.3. *Absorption Features*

A few continuum sources can be seen in absorption. Most notable among the compact sources are those at (136°.21, $-0°.90$), (132°.06, 0°.21), and (131°.46, 1°.16), best seen in Figure 4*a*. The first of these corresponds to 3C 69. The most prominent absorption features are those associated with W3, which can be seen out to $v = -50$ km s^{-1}. There are three main absorption peaks along this line of sight: one corresponding to local gas, one corresponding to the Perseus arm, and an intermediate peak centered on -22 km s^{-1}. Figure 7 shows the absorption profiles associated with W3 N (*dashed line*) and W3 W (*dotted line*) along with an emission spectrum of the surrounding gas (*solid line*). The emission spectrum is the average for an annulus of inner radius 12'.5 and outer radius 22'.5 centered on W3. The absorption spectra are averages of all pixels for which the 1420 MHz continuum value is greater than 100 K in the W3 N and W3 W regions. Read (1981) has argued that the Perseus arm absorption stems from gas that is associated with W3. It is interesting that there is H I emission at velocities between the intermediate and Perseus arm absorption peaks, at $v \sim -30$ km s^{-1}. This suggests that this gas is displaced in velocity, i.e., that it is not following the rotation curve of the Galaxy. The lack of absorption places it behind the W3 region, and the less negative velocity indicates that it is approaching us with a velocity of at least -19 km s^{-1} relative to the rotation curve, as determined from the lower velocity limit of the W3 absorption and the upper velocity limit of this emission peculiarity.

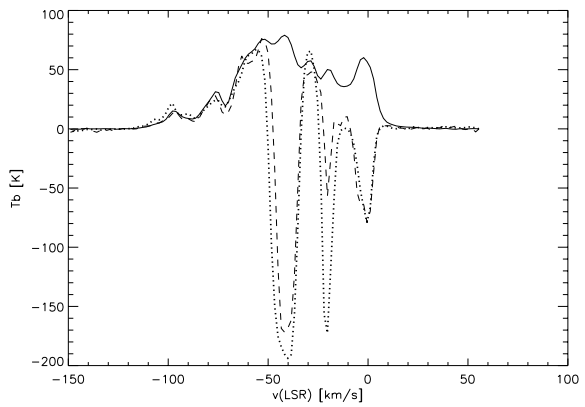

FIG. 7.—H I absorption of W3 N and W3 W. H I spectra along a line of sight toward W3 N (*dashed line*) and W3 W (*dotted line*) are plotted along with the average emission spectrum of the surrounding gas (from an annulus with an inner radius of 12'.5 and an outer radius of 22'.5). The absorption spectra were obtained by averaging the H I images for all pixels for which the continuum values were greater than 100 K, at the positions of W3 N and W3 W.

In addition to the absorption of compact continuum sources, there appear to be self-absorption features, in the form of arcs and filaments of lesser intensity in areas of bright emission, wherein colder foreground H I absorbs the emission from more distant atomic hydrogen. These are seen in the velocity range corresponding to the Perseus arm. From -35.2 to -41.8 km s^{-1} there are extended arcs of self-absorption just below and overlapping the eastern portion of W5. For -35.2 to -53.3 km s^{-1}, there are self-absorption features to the south of W4 and HB 3, beginning to the southeast of W4 and generally progressing westward as one moves through the velocity interval. Deciding what is self-absorption and what is simply a lack of emission is somewhat subjective. We identify as evidence of self-absorption dark features with sharp edges, seen against bright H I emission, that do not correspond to features in the continuum emission (see, e.g., at $v = -49.18$ km s^{-1}, the large, 0°.9 × 1°.8, fan-shaped feature below W4 in Fig. 4*e*). In the Perseus arm velocity interval, where the emission is bright over the entire mosaic, self-absorption features stand out as distinct from low-emission areas. The self-absorption features are far more evident in the electronic versions of the images, and the interested reader should examine them on the Web site, where, for example, the fan-shaped feature is best seen at -48.35 km s^{-1}.

5.2. H I *Associated with the Perseus Complex*

5.2.1. *W3*

Read (1981) analyzed H I aperture synthesis observations toward W3. His data have a similar spatial resolution to those presented here and a somewhat coarser velocity resolution; however, they are restricted to a 1° radius area around W3. Many structures seen by Read also appear in this data set, but with the help of the larger field of view, some are now shown to be part of larger scale structures. In particular, the large diffuse cloud 20′–30′ to the south of W3 in the -50 to -54 km s^{-1} range is seen here to be part of a larger scale extended structure, likely not associated with the H II region. As well, Read's feature 4, an arc of emission at -24 km s^{-1}, is seen to be part of an extended ridge of emission. It is not clear where one should draw the boundaries for this ridge: it can be seen as an arc extending from (133°.3, 0°.4) to (134°.7, 2°.5) or as part of a longer filament that diagonally traverses most of the mosaic. Again, it is unlikely that such a large-scale feature would be associated with the compact W3 region. A third feature mentioned by Read upon which the larger field of view sheds new light is "an area of emission about 1° east-west by 1.5° north-south which surrounds W3 and W3N" between -35 and -45 km s^{-1}. On the images presented here, it becomes apparent that this is not so much H I emission associated with W3 as absences of emission associated with HB 3 to the west and above W4 to the east. In other words, there is a "peninsula" of H I at the position of W3, attached to a broad region of emission to the south, and extending in between regions where the H I has been evacuated by HB 3 and W4 (see below).

5.2.2. *W4*

Above the W4 H II region, there is a conical void in the H I distribution, centered on -43 km s^{-1}. Braunsfurth (1983) suggested the presence of an expanding H I shell around W4. The data used by Braunsfurth did not extend as high in latitude as do the observations presented here,

leading the author to interpret a concentration of H I emission at $l = 2.^{\circ}0$ as the upper boundary of the shell. With the help of the larger field of view, this is seen to be a feature within a larger cavity. This whole structure is proposed to correspond to a Galactic chimney blown by the OCl 352 open star cluster (Normandeau et al. 1996). The cluster contains nine O stars, which input sufficient energy into the ISM via stellar winds to account for the formation of the chimney. From the age of the cluster and by use of simple models of superbubble evolution, it was estimated that the chimney is just in the process of blowing out of the Galactic plane.

Below and to either side of W4, there are no obviously related H I features. At best, a case could perhaps be made for H I tracing the southwest of the region within a narrow range of velocities centered on -60 km s^{-1}. As well, some of the self-absorption features described earlier seem to follow the southern outline of the H II region somewhat, to fan out around it.

5.2.3. *W5*

The W5 H II region does not seem to have an associated expanding shell of H I, although, because of its location at the edge of the mosaic, it is possible that such a structure would go unnoticed. There is however H I that traces the western boundary of the region between -24 and -30 km s^{-1}, supporting the suggestion made earlier, in the discussion of the absence of a continuum halo (§ 4.3), that W5 is ionization bounded.

5.2.4. *HB 3*

The H I environment of the SNR HB 3 was studied by Routledge et al. (1991) using the DRAO ST. The present data offer a wider field of view, which is useful for the larger scale structures and placing them in context. The most striking feature is the large H I shell that encircles the continuum emission. Routledge et al. saw this feature in a single channel, at -29 km s^{-1}, and it is at this velocity that it is most apparent in this data set, but with the contrast provided by the larger field of view, it can now be seen to extend in velocity from -25 to -43 km s^{-1}, varying somewhat in size along the way. This overlaps with Read's interval of -27 to -34 km s^{-1} for an arc to the northwest of W3 that he linked to HB 3.

6. CONCLUSION

The observations presented here constitute the pilot project for the DRAO Galactic plane survey. The observing and data reduction techniques served as a blueprint for the now ongoing survey of the northern Galactic plane, and some modifications suggested themselves as a result of the gained experience. In particular, for the full survey, the field centers are closer together in order to reduce the effects of the noticeably increased noise at the edges of the individual fields on the H I mosaic. It should also be noted that the DRAO ST is now equipped with 256-channel spectrometers, thus improving the velocity resolution by a factor of 2 for the same velocity coverage. Also, there is a sufficient number of these new spectrometers to allow both RR and LL observations simultaneously, the result of which will be a reduction of noise level for the H I images. Data-processing software development was catalyzed by the pilot project, and it is now possible to remove artifacts related to strong sources such as W3.

The data resulting from the pilot project observations of the W3/W4/W5/HB 3 Galactic complex show this region at high resolution with a large field of view. For the H I spectral line, this data set constitutes an order-of-magnitude improvement in spatial resolution over the best previous H I images of the entire complex. A wealth of intriguing features have been brought to light. Long, thin H I filaments are shown to be common in the Galaxy, many of them extending over several degrees. Particularly intriguing are filaments at extreme negative velocities that are not quite aligned with the Galactic plane. The combination of good spatial resolution and field of view also shed light on H I structures associated with the continuum-emitting gas, putting into context some features previously thought to be associated with W3 and highlighting some associated with HB 3 that are far less obvious when the field of view is smaller.

The data are best viewed in digital form and can be found on the World Wide Web at ⟨http://www.ras.ucalgary.ca/pilot_project.html⟩. Furthermore, as indicated on the Web page, FITS files of the data can be requested from the authors. The data will eventually become available on CD-ROM, as well as from a standard astronomical archive site.

Many members of the DRAO staff were helpful during observations and data reduction. In particular, T. L. Landecker participated in many enlightening discussions, for which M. N. is very grateful. The Dominion Radio Astrophysical Observatory's synthesis telescope is operated by the National Research Council of Canada as a national facility. This research has made use of the SIMBAD database, operated at CDS, Strasbourg, France, and of NASA's Astrophysics Data System Astrophysics Science Information and Abstract Service.

REFERENCES

Baars, J. W. M., Genzel, R., Pauliny-Toth, I. I. K., & Witzel, A. 1977, A&A, 61, 99
Brand, J., et al. 1994, A&AS, 103, 541
Braunsfurth, E. 1983, A&A, 117, 297
Caswell, J. L. 1967, MNRAS, 136, 11
Clark, B. G. 1980, A&A, 89, 377
Dickel, H. R. 1980, ApJ, 238, 829
Dickel, H. R., Dickel, J. R., Wilson, W. J., & Werner, M. W. 1980, ApJ, 237, 711
Dickel, H. R., Harten, R. H., & Gull, T. R. 1983, A&A, 125, 320
Digel, S. W., Lyder, D. A., Philbrick, A. J., Puche, D., & Thaddeus, P. 1996, ApJ, 468, 561
Elmegreen, D. M. 1980, ApJ, 240, 846
Fesen, R. A., Downes, R. A., Wallace, D., & Normandeau, M. 1995, AJ, 110, 2876
Fürst, E., Reich, W., Reich, P., & Reif, K. 1990, A&A, 85, 691
Garmany, C. D., & Stencel, R. E. 1992, A&AS, 94, 211
Gray, A. D., Landecker, T. L., Normandeau, M., Taylor, A. R., & Dewdney, P. E. 1996, in preparation
Haslam, C. G. T., Salter, C. J., Stoffel, H., & Wilson, W. E. 1982, A&AS, 47, 1
Kallas, E., & Reich, W. 1980, A&AS, 42, 227
Landecker, T. L., Vaneldik, J. F., Dewdney, P. E., & Routledge, D. 1987, AJ, 94, 111
Normandeau, M., Taylor, A. R., & Dewdney, P. E. 1996, Nature, 380, 687
Ogura, K., & Ishida, K. 1976, PASJ, 28, 650
Oldham, P. G., Griffin, M. J., Richardson, K. J., & Sandell, G. 1994, A&A, 284, 559
Palagi, F., Cesaroni, R., Comoretto, G., Felli, M., & Natale, V. 1993, A&AS, 101, 153
Read, P. L. 1981, MNRAS, 194, 863
Reich, W. 1982, A&AS, 48, 219
Roelfsema, P. R., & Goss, W. M. 1991, A&AS, 87, 177

Routledge, D., Dewdney, P. E., Landecker, T. L., & Vaneldik, J. F. 1991, A&A, 247, 529
Sajn, G. A. 1954, AZh, 31, 217
Steer, D. G., Dewdney, P. E., & Ito, M. R. 1984, A&A, 137, 159
Strobel, A. 1992, A&A, 253, 374
Thronson, H. A., Jr., Lada, C. J., & Hewagama, T. 1985, ApJ, 297, 662
Williams, D. R. W. 1973, A&AS, 8, 505
Wynn-Williams, C. G., Becklin, E. E., & Neugebauer, G. 1972, MNRAS, 160, 1